# Convection and Heat Transfer in Island (Warm) Wakes

CÁTIA C. AZEVEDO,[a,b] CAROLINA M. L. CAMARGO,[c] JOSÉ ALVES,[a,b] AND RUI M. A. CALDEIRA[a,b]

[a] *Oceanic Observatory of Madeira, ARDITI, Funchal, Portugal*
[b] *Dom Luiz Institute, Faculty of Sciences, University of Lisbon, Lisbon, Portugal*
[c] *Royal Netherlands Institute for Sea Research (NIOZ), Yerseke, Netherlands*

(Manuscript received 15 May 2020, in final form 19 December 2020)

ABSTRACT: The interaction between the incoming winds and high mountainous islands produces a wind-sheltered area on the leeward side, known as the atmospheric wake. In addition to weaker winds, the wake is also characterized by a clearing of clouds, resulting in intense solar radiation reaching the sea surface. As a consequence, a warm oceanic wake forms on the leeward side. This phenomenon, detectable from space, can extend 100 km offshore of Madeira, where the sea surface temperature can be 4°C higher than the surrounding oceanic waters. This study considers in situ, remote sensing, and ocean circulation model data to investigate the effects of the warm wake in the vertical structure of the upper ocean. To characterize the convective layer (25–70 m) developing within the oceanic wake, 200 vertical profiles of temperature, salinity, and turbulence were considered, together with the computation of the density ratio and Turner angle. In comparison with the open-ocean water column, wake waters are strongly stratified with respect to temperature, although highly unstable. The vertical profiles of salinity show distinct water parcels that sink and/or rise as a response to the intense heat fluxes. During the night, the ocean surface cools, leading to the stretching of the mixed layer, which was replicated by the ocean circulation model. In exposed, nonwake regions, however, particularly on the southeast and north coasts of the island, the stretching of the mixed layer is not detectable.

KEYWORDS: Atmosphere-ocean interaction; Convection; Turbulence; Oceanic mixed layer; Sea surface temperature; Buoyancy; Evaporation; Radiative forcing; Surface fluxes; Thermodynamics; Coupled models; Orographic effects; Wind effects

## 1. Introduction

In a strongly stratified atmosphere, a mountainous island forces the striking airflow to split, generating a wake of weak winds downstream and stronger-than-ambient winds on the flanks (i.e., Venturi effect; Xie et al. 2001; Alves et al. 2020). Island wakes can take one of many forms, depending on the large-scale wind, temperature profiles, and mountain height. Shedding of atmospheric vortices in the lee side leads to low cloud cover inside the wake, exposing the sea surface to intense solar radiation during the day (Caldeira et al. 2002; Yang et al. 2008). These conditions induce sea surface warming and enhance evaporation (Xie et al. 2001). Wakes of "warm water" have been observed using satellite derived sea surface temperature (SST) maps offshore the Hawaiian Islands (Xie et al. 2001; Yang et al. 2008), on the southwest of La Palma, Gomera, Hierro, Tenerife, and Gran Canaria (e.g., Van Camp et al. 1991) and in the lee of Madeira Island (Caldeira et al. 2002). The latter is characterized by an increased in SST of up to 4°C, relative to the surrounding oceanic waters, developing during late spring to early summer. Most often, the warm wake forms in the south coast (leeward) of the island, parallel to the dominant trade winds direction. North coast episodes are known to occur when the wind blows from the south for more than five consecutive days (Caldeira et al. 2002).

Besides the dynamic effects of the airflow often manifested in the form of wind stress curl, the thermal forcing can also impact the local ocean circulation. Heat transfer is high, particularly in areas with weak surface winds and thus weaker mixing as in the lee of islands (e.g., Yang et al. 2008). However, the thermodynamic effects of wakes are poorly discussed in the scientific literature. Most studies focus on the (dominant) transfer of momentum from the atmospheric to the ocean surface (e.g., Dong and McWilliams 2007; Couvelard et al. 2012), often disregarding the thermal contributions (Caldeira and Tomé 2013; Caldeira et al. 2014).

Ocean circulation driven by atmosphere–sea interaction processes, such as convection, are common within the ocean mixed layer (Kantha and Clayson 2002). These can develop due to a loss of heat from the surface to the atmosphere and/or due to an increase in salinity caused by an increased evaporation. In a stratified water column—where temperature and salinity decrease with depth—the density gradient between layers is high and evaporation dominates over precipitation, creating the conditions for salt-finger formation (Kantha and Clayson 2002; Pérez-Santos et al. 2014; Arnon et al. 2016). The regime of salt-finger requires a destabilizing salinity profile and a compensating stabilizing temperature profile (Zodiatis and Gasparini 1996). This destabilization may arise from small salinity gradients, since the salt diffusivity is two orders of magnitude below the thermal

Denotes content that is immediately available upon publication as open access.

Supplemental information related to this paper is available at the Journals Online website: https://doi.org/10.1175/JPO-D-20-0103.s1.

*Corresponding author*: Rui Caldeira, rui.caldeira@oom.arditi.pt

DOI: 10.1175/JPO-D-20-0103.1

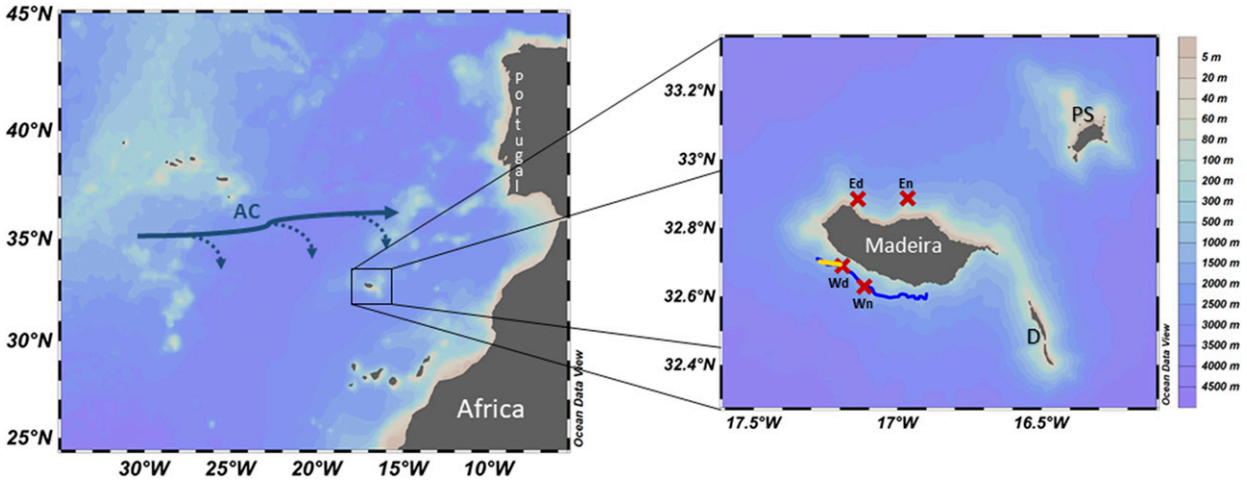


FIG. 1. Location of the archipelago in the northeast Atlantic Basin, with Madeira, Porto Santo (PS), and Desertas (D) Islands, including the location of the sampling stations in exposed (Ed and En) and sheltered (Wd and Wn) regions. The blue line represents the transect at the 1000-m bathymetric, and the yellow line is the Wirewalker sampling drift. The Azores Current (AC) is represented on the left panel as the main surface oceanic feature affecting the archipelago.

conductivity ($\sim 1.1 \times 10^{-9}$ and $\sim 1.4 \times 10^{-7}\,m^2\,s^{-1}$, respectively). Therefore, vertical convection occurs when parcels of warmer and more saline water sink into less warm and fresher waters (Stern 1960; Schmitt 2003; Radko 2013; Rehman and Singh 2017). The phenomenon can also arise when the density stratification is continuous, concurrent with slower salty diffusivity (Schmitt 2003). Under such conditions the contribution of downward salt flux to the density flux exceeds that of heat, and therefore the transport of salt controls the direction of the net density flux (Radko 2013). You (2002) suggested that the phenomenon of salt-finger formation is stronger in the North Atlantic Ocean than it is in the Pacific and Indian Oceans, with subtropical latitudes having the most favorable conditions. However, the study of this phenomenon has been mostly confined to laboratory and/or numerical studies (e.g., Tippins and Tomczak 2003; Hage and Tilgner 2010; Rehman and Singh 2017; Ouillon et al. 2019), with some discussions including observational data (Schmitt 1981, 2003; Zodiatis and Gasparini 1996; Holbrook et al. 2003; Pérez-Santos et al. 2014; Nagai et al. 2015; Arnon et al. 2016).

This study uses observations and numerical simulations to characterize the convective processes that develop within the warm wake of Madeira Island (Fig. 1). Following the introduction, the paper is organized as follows: section 2 describes the instruments, datasets, and methods. Section 3 uses satellite observations to characterize the environmental settings, including the regional atmospheric dynamics and its implications in the SST. Section 4 presents the results, consisting of observations and numerical model solutions. Section 5 discusses and summarizes the main findings.

## 2. Instruments, datasets, and methods

### a. Oceanographic campaign

There were two oceanographic summer campaigns, one during 2017 (13–30 August) and another in 2018 (4–27 July). The ship-based measurements included synoptic transects, stations profiles, as well as the deployment of an autonomous vehicle, that is, the Wirewalker. Several instruments were used to capture the response of the ocean's interior to the atmospheric forcing. Satellite and numerical model solutions complemented the in situ measurements.

Between 13 and 30 August 2017, an oceanographic campaign on board the research vessel (R/V) *SOCIB* sampled four stations (Fig. 1; Ed and En north side of the island and Wd and Wn on the leeward side); a total of 116 temperature, salinity profile, and turbulence measurements were collected. These were carried out using a conductivity–temperature–depth profiler (SeaBird-19 pumped CTD) and a vertical microstructure profiler (Rockland Scientific VMP-250). An underway CTD (uCTD; Oceanscience) was also used in an attempt to achieve a synoptic characterization of the warm wake (transect represented by blue line in Fig. 1). Both instruments carried calibrated sensors.

During the July of 2018 campaign, an autonomous vehicle fitted with a CTD and a turbulence microstructure profiler was deployed in the oceanic warm wake region (Del Mar Oceanographic Wirewalker). The following sections detail the processing of the acquired data [section 2a(1)], the physical quantities calculated [section 2a(2)], and the statistical analysis [section 2a(3)].

#### 1) Data acquisition and processing

##### *(i) CTD profiler*

The CTD profiler sampled data at 4 Hz and collected 20 profiles in the wake region and 18 in the open-ocean region. The acquisition was carried out using the Seaterm software, and the processing included a set of SBE Data Processing routines (Sea-Bird Electronics). The recommended processing procedures for our probe model (SBE-19 plus) included 1) the conversion of binary data to physical variables; 2) filtration, that is, definition of the maximum and minimum limits for pressure, temperature, and conductivity; the rectification of temperature and conductivity sensors in relation to pressure

(to guarantee the sampling the same water parcel); 3) the correction of the effect of thermal mass of the cell; as well as 4) the derivation of other physical variables, such as salinity and density. The data visualization was done using Python routines.

*(ii) Vertical microstructure profiler*

The microscale velocity shear was obtained using the VMP-250 with an acquisition frequency of 512 Hz, with 38 profiles at the four stations. Data were processed using the Oceanographic Data Acquisition System software (Rockland Scientific ODAS5-IR) such that, first, the power of spectrum of the shear velocity was calculated for each 8- and 10-s segment, by block-averaging fast Fourier transform, considering segments with 2 and 3 s, with a 50% overlap, for profiles with 150 and 300 m, respectively [as used in Itoh et al. (2010), Tanaka et al. (2015), and Lueck and Murowinski (2017)]. The rate of dissipation of turbulent kinetic energy $\varepsilon$ was obtained by integrating the spectra of the velocity shear (Lueck 2016), using the equation

$$\varepsilon = \frac{15}{2}\nu\left(\frac{\partial u}{\partial z}\right)^2 = \frac{15}{2}\nu\int_0^\infty \psi(k)\,dK, \tag{1}$$

where $\psi$ is the spectrum of the shear $\partial u/\partial z$, $\nu$ is the kinematic molecular viscosity, and $k$ is the wavenumber. The integration is done over wavenumbers from 0 cycles per meter (cpm) to the Kolmogorov number (Lueck and Murowinski 2017). The upper limit of the integration was automatically adjusted for each profile. A low-pass smoothing filter (Butterworth) was applied in all profiles (Lueck and Murowinski 2017) by manually adjusting the parameters (e.g., spike identification threshold, cutoff frequency, and number of removed data after the identification of a spike) to remove noise and obtain a spectrum that fit well with the Nasmyth universal spectrum (Tanaka et al. 2015). The rates of dissipation were calculated from the two shear probes and averaged into one $\varepsilon$ per segment.

*(iii) Underway CTD*

The uCTD was operated in "tow-yo" mode, measuring from the ocean surface down to 225 m depth, along the 1000 m bathymetric isoline. Operating at 16 Hz, the high-resolution synoptic sampling (vertical dives every 1 km), acquired a total of 40 profiles of the water column. The data collected by the uCTD were processed according to the method developed by Ullman and Hebert (2014), as detailed in the online supplemental material. In brief, there is a lag between the conductivity and temperature measurements when the instrument has a low descent rate (as it is in our case), thus the conductivity measurements must be advanced relative to the temperature readings. Because the uCTD can profile at descent rates greater than 4 dbar $s^{-1}$, the effect of viscous heating of the thermistor is nonnegligible, and therefore temperature should be corrected for this effect, prior to computing salinity (Mensah et al. 2009; Ullman and Hebert 2014; Mensah et al. 2018).

*(iv) Autonomous vehicle: The Wirewalker*

The Wirewalker is an autonomous vertical profiler instrument that uses ocean waves and buoyancy for its vertical displacements (Pinkel et al. 2011). Profiling extends the one-dimensional time series recording of the instrument to a two-dimensional depth–time record. For the vertical characterization of the water column, a CTD (RBRconcerto[3], sampling at 6 Hz) was attached to the profiler. During 23 and 24 July, the equipment spent a total of 19 h drifting in the warm wake region while registering 84 profiles. One advantage of the autonomous profiler relative to ship-based measures is that it is capable of sampling an undisturbed water column, since the ship displacement disturbs the ocean surface resulting in valid profiles only below 10-m depth. Nevertheless, the best data are collected during the free (uninterrupted) ascent, with upward speeds of 0.24–0.5 m $s^{-1}$ (Pinkel et al. 2011); therefore, only the ascending casts were considered herein.

2) CALCULATIONS OF PHYSICAL QUANTITIES

To better interpret the dissipation data, the vertical shear of horizontal velocity $S = [(\partial u/\partial z)^2 + (\partial v/\partial z)^2]^{1/2}$, the squared of the buoyancy frequency $N^2 = (-g/\rho_0)(d\rho/dz)$, the diapycnal diffusivity $K_\rho = 0.2 \times \varepsilon/N^2$, and the Richardson number $\mathrm{Ri} = N^2/S^2$ were also calculated (Osborn 1980; Itoh et al. 2010; Tanaka et al. 2015; Galperin et al. 2007).

The vertical stability ratio $R_\rho$ and the Turner angle Tu were calculated to identify salt-finger convection and diffusive convection phenomena. The ratio $R_\rho$ (Turner 1973), with a contribution of temperature and salinity (Tippins and Tomczak 2003), is defined as

$$R_\rho = \frac{\alpha^\Theta \Theta_z}{\beta^\Theta (S_\mathrm{A})_z}, \tag{2}$$

where $\alpha^\Theta = \rho^{-1}(\delta\rho/\delta\theta)$ is the thermal expansion coefficient, $\beta^\Theta = -\rho^{-1}(\delta\rho/\delta S_\mathrm{A})$ is the haline contraction coefficient, $\rho$ is the density of seawater, $\Theta$ is the Conservative Temperature, and $S_\mathrm{A}$ is the Absolute Salinity. The Turner angle was used to verify the existence of salt-fingering/diffusive convection phenomena (Ruddick 1983) and to quantify the influence of temperature and salinity on the water column (Pérez-Santos et al. 2014) and is defined as

$$\mathrm{Tu} = \tan^{-1}\left(\frac{R_p + 1}{R_p - 1}\right). \tag{3}$$

When Tu is between −45° and 45° the water column is stable with regard to temperature and salinity. When Tu is between 45° and 90° ($R_\rho$ between 1 and $+\infty$) the conditions are concurrent with the formation of salt-fingering, whereas when Tu varies between −90° and −45° ($0 < R_\rho < 1$) the region is predisposed to diffusive convection.

The vertically integrated heat content (Na et al. 2012) was also calculated as

$$\mathrm{HC} = \rho_0 c_p \int_{h2}^{h1} T_z\, d_z, \tag{4}$$

where $c_p$ is the specific heat capacity at constant pressure, $T$ is the temperature, and $h$ is the water depth.

3) STATISTICAL ANALYSIS

To obtain a representative value, all of the profiles for each station (CTD and VMP data) were time averaged by the

bootstrap method, considering a 95% confidence interval. The bootstrap is a nonparametric method that provides a robust estimation of the statistical error. Based on the Monte Carlo method, the bootstrap draws several random samples ($B$ replicates), with replacement, from the original dataset (Efron and Gong 1983). The sample number from the original dataset, in this case the number of profiles per station, provides the degree of freedom of the statistic (St. Laurent et al. 2012). A large number of bootstrap replicates ($B = 1000$) was used so as to achieve a reliable estimation. This method was employed to obtain the error distribution for the $\varepsilon$, $K_\rho$, $S^2$, $N^2$, Tu, $R_\rho$, and HC and for the physical parameters (temperature, salinity, and density).

### b. Satellite data

Wind, SST, and irradiance data collected using satellites were processed for the study period. Fast-evolving, small-scale features over the ocean require high-resolution wind data. The European Organisation for the Exploitation of Meteorological Satellites (EUMETSAT) Ocean and Sea Ice Satellite Application Facility (OSI SAF) produces a range of air–sea interface products, such as wind, SST, and radiative fluxes (i.e., surface solar irradiance and downward longwave irradiance). The measurements are obtained through the processing of scatterometer data from the ASCAT instrument flying on board EUMETSAT's *MetOp-A*. The ASCAT wind product contains measurements of wind speed and direction above the sea surface (~10 m), at 12.5-km spatial resolution. Verhoef et al. (2012) compared the scatterometer wind data (12.5 and 25 km) with in situ wind data from moored buoys. Their results showed that the 12.5-km winds have slightly lower standard deviations of the wind component (zonal and meridional) when compared with the 25-km wind products.

The SST is one of the most important proxies of the oceanic warm wake. The ocean emits radiation in the infrared and microwave wavelengths. The amplitude of these wavelengths varies with the temperature of the ocean and therefore can be used to derive SST. EUMETSAT produces SST products in near-real-time from MetOp and AVHRR infrared sensors installed on board polar-orbiting satellites. Passive infrared sensors have better spatial resolution but are susceptible to cloud contamination resulting from the absorption of the infrared energy emitted by clouds that are often masked in SST maps (Minnett et al. 2019). The MetOp/AVHRR combined product is delivered at full resolution in satellite projection as a metagranule corresponding to a 3-min-resolution (~5.5 km) dataset. The *MetOp-B*/AVHRR data were validated by Saux Picart et al. (2015) using three independent datasets: the Global MetOp Sea Surface Temperature, the North Atlantic Regional Sea Surface Temperature, and the Full Resolution MetOp Sea Surface Temperature from drifting buoys. Their results showed that the *MetOp-B*/AVHRR data are accurate and very stable. Therefore, for this study, the MetOp Sea Surface Temperature product with 1-km spatial resolution at nadir was used.

For the radiative fluxes, the operational chain uses data from GOES-E, Meteosat (geostationary at 0°E), and *Meteosat-8*. The solar irradiance at the surface is a function of the solar irradiance at the top of the atmosphere, the clear sky atmospheric transmittance and the combined effects of clouds, which is a function of the cloud albedo (Godøy 2016). The product is remapped onto a 0.05° regular grid and is expressed in watts per meter squared. The validation of this product by Marsouin (2017) showed that the *Meteosat-8* error statistics compare favorably to the measurements (*GOES-13* and *Meteosat-10*), with standard deviations lower than the operational products.

### c. Numerical simulations

Some studies rely on hydrodynamic models to complement observations of convective processes (e.g., Ouillon et al. 2019). Here a coupled modeling system was used as a first attempt to resolve the warm-wake observations considering heat and momentum transfers at the air–sea interface.

To study the dynamics of the air–sea interaction in warm wake conditions at a high temporal (1 h) and spatial (1 km) resolutions, the COAWST (Coupled Ocean Atmosphere Wave Sediment Transport) numerical system was used, such that the Weather Research and Forecasting (WRF) Model represented the atmospheric conditions and the Regional Ocean Circulation Model (ROMS) represented the ocean response. WRF provided a 10-m surface wind, atmospheric surface pressure, relative humidity, atmospheric surface temperature, precipitation, and net shortwave and longwave fluxes to ROMS, whereas the latter provided SST to the atmospheric model. The variables are exchanged every 30 model minutes, using the Modeling Coupling Toolkit (MCT). For a comprehensive description of the COAWST, the reader is referred to Warner et al. (2008a,b, 2010). COAWST was successfully used in previous Madeira wake studies (Pullen et al. 2017a; Alves et al. 2020).

As in previous studies, WRF used 60 terrain-following vertical levels, with increasing resolution near the surface, with the lowest midcell level at approximately 14 m above sea level, and 15 levels below 1400 m, in order to accurately simulate the near-surface wind vertical structure. ROMS considered 40 sigma vertical levels, with increasing vertical resolution near the ocean surface. WRF is a fully compressible and nonhydrostatic model. A detailed description of the model can be found in Skamarock et al. (2008). The initial and boundary atmospheric conditions were retrieved from ERA5 (Copernicus Climate Change Service 2017), a European Centre for Medium Weather Forecast (ECMWF) reanalysis dataset, with outputs every 3 h. To represent the island topography, the Shuttle Radar Topography Mission (SRTM) data with a 3-arc-s resolution was used. Moreover, for an accurate representation of the land use, which varies to a great degree around the island, we used the Coordinated Information on the Environment (CORINE) land cover dataset. For WRF parameterizations the following options were considered: the WRF Single-Moment 6-class scheme (Hong et al. 2004) was used to simulate the clouds microphysics. For longwave radiation we used the Rapid Radiative Transfer Model (Mlawer et al. 1997), and for shortwave radiation the Dudhia scheme (Dudhia 1989) was considered. The surface layer followed the ETA similarity scheme (Janjić 1996, 2002), and the planetary boundary layer used the Mellor–Yamada–Janjić scheme (Janjić 1990, 1994). Slope and shading effects were only considered in the 1-km inner domain. Validated applications of WRF to study the Madeira wakes using similar

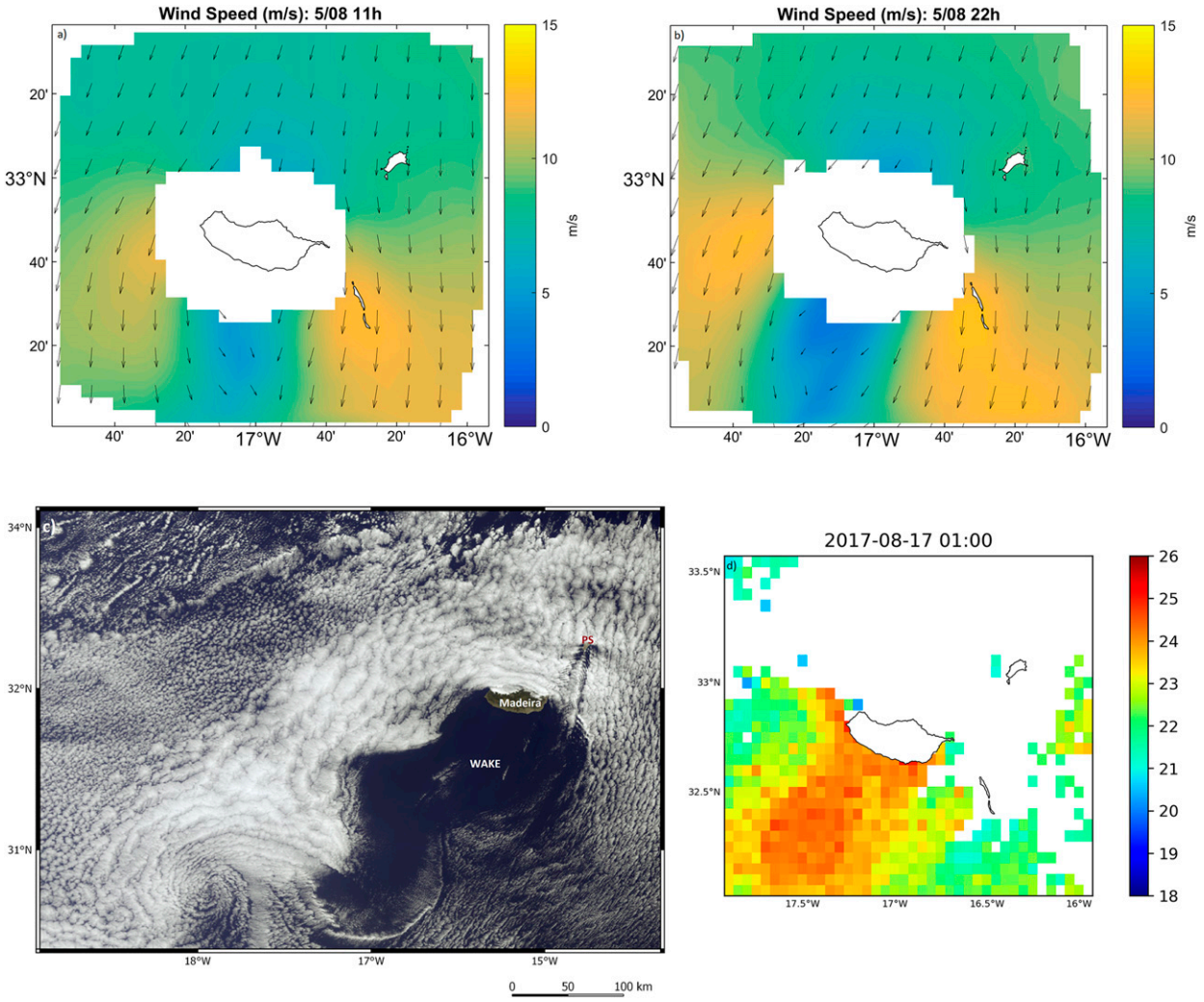


FIG. 2. ASCAT wind data direction (vectors) and speed (colors; m $s^{-1}$) for (a) day and (b) night. (c) *Sentinel-3A* (level 1) visible-band full-resolution image of Madeira, collected at 1104 UTC 18 Aug 2017, showing the atmospheric von Kármán vortex street (wake), associated with the clearing of clouds over the ocean on the leeward side. (d) MetOp/AVHRR data showing SST (°C).

parameterizations include Couvelard et al. (2012), Caldeira and Tomé (2013), and Grubišić et al. (2015).

ROMS is a free-surface, terrain-following, primitive equations model with the hydrostatic and Boussinesq approximations. A description of the ROMS model is detailed in Shchepetkin and McWilliams (2005, 2009). Radiation and nudging boundary conditions were imposed for tracers (temperature and salinity) and baroclinic velocities (Marchesiello et al. 2001), a Shchepetkin condition for barotropic velocities (Mason et al. 2010) and a Chapman condition for free-surface height (Chapman 1985). Vertical turbulent mixing was parameterized with a two-equation turbulence scheme, using the generic length scale (GLS) proposed by Umlauf and Burchard (2003) and implemented in ROMS by Warner et al. (2005). Turbulence is represented by a $k$–$\varepsilon$ closure, where $k$ is the turbulent kinetic energy and $\varepsilon$ is dissipation. The tidal forcing considered the Oregon State University tidal constituents. Oceanic initial and boundary conditions were based on 24-h intervals of the Hybrid Coordinate Ocean Model (HYCOM), which also included the Navy Coupled Ocean Data Assimilation (NCODA) global analysis data, in a 1/12° resolution. Raw bathymetry data were extracted from a 30-arc-s grid spacing, using the General Bathymetric Chart of the Oceans (GEBCO). Several passes of a smoothing filter guaranteed a bathymetry $r$ factor ($r = \nabla h/h$) below 0.2, ensuring stability of sigma coordinate calculations (Haidvogel and Beckmann 1999). Successfully uses of ROMS to study the Madeira wake include Caldeira and Sangrà (2012), Couvelard et al. (2012), and Caldeira et al. (2016).

## 3. Environmental settings

Madeira Island (Fig. 1) is located in the northeast Atlantic Ocean (32.5°N, 17°W), approximately 850 km offshore from the southwest tip of Portugal. This northwest–southeast-oriented island is 55 km long and approximately 25 km wide.

The island has a mountain chain of volcanic origin that dominates the interior orography, with a large portion above 900 m of altitude, and with the highest peak standing at 1800 m above sea level. A recent 40-yr (1979–2018) atmospheric numerical simulation (unpublished) showed that the mean summer (July–September) surface wind direction is predominantly from the northeast quadrant, but occasionally can veer east.

In terms of wind stress curl, the region around the island is characterized by a negative (anticyclonic) wind stress curl near the eastern flank, and a positive wind stress curl (cyclonic) on the western flank. Couvelard et al. (2012) discussed the oceanic implications of these wind curl features at the island flanks, which included momentum transfer and the formation of oceanic vortices. Figures 2a and 2b represent the intensity and direction of the wind for the period of the oceanographic campaign. The wind was predominantly from the north quadrant, with speeds ranging from 2 to 11 m $s^{-1}$. During the summer months, the position of the Azores high influences the wind pattern in the Madeira region, resulting in an incoming northwest flow interacting perpendicularly with the island mountain chain. In addition, during this time of year the strong trade wind inversions lie below the Madeira central mountain top [refer to climatological study in Grubišić et al. (2015)]. These two elements together constitute the optimal conditions for the formation of an (almost permanent) von Kármán vortex street in the atmosphere (Caldeira and Tomé 2013; Grubišić et al. 2015). The resulting wake appears as a zone of reduced momentum and an accelerated flow at the outer flanks, that is, jets (Figs. 2a,b) (Grubišić et al. 2015; Alves et al. 2020). The interior of the atmospheric wake is characterized by weaker winds and frequent changes in its direction. Despite the intensification of the night mountain breezes (down-valley winds), the wake region remains mostly unperturbed throughout the day (Pullen et al. 2017b).

The cloud-free conditions in the lee side of Madeira makes the effect of the wake on the atmosphere visible from space (Hubert and Krueger 1962), as shown in Fig. 2c. Several studies have noted that the impact of Madeira's topography is not limited to the atmospheric flow leeward of the island, generating a pool of warm water in the surface of the ocean. The absence of clouds and weaker winds on the lee side are expected to suppress ocean mixing, further contributing to the warming of the sea surface (Caldeira et al. 2002; Caldeira and Tomé 2013; Grubišić et al. 2015). In addition, Caldeira et al. (2002) reported differences of temperature on the order of 4°C between the wake region and surrounding oceanic waters. The SST records (dataset with 1-km resolution; Fig. 2d) show one area with absence of clouds concurrent with sea surface temperatures close to 25°C. In contrast, the temperatures of the surrounding oceanic waters varied between 21° and 22°C.

## 4. Results

### a. Solar irradiance and sea surface temperature

Considering that solar irradiance is one of the main forcing mechanisms for the establishment of the oceanic warm wake, the processed satellite data took into account exposed (nonwake) and sheltered (wake) regions (Fig. 1, Ed/En and Wd/Wn, respectively). Heat is added to the ocean through shortwave radiation, and lost via latent, sensible heat fluxes and longwave radiation. Shortwave radiation is not absorbed in the ocean surface skin layer, instead it can penetrate as deep as 100 m, depending on the wind stirring effect and on the magnitude of the incident radiation flux (Talley et al. 2011). Figure 3 represents the daily variation of the downwelling shortwave and longwave radiation (Figs. 3a,b, respectively). Shortwave radiation reaches the sea surface differently in the two areas, with maximum values in the sheltered zone (~1000 W $m^{-2}$ at 1300 UTC), and less available incident radiation in the exposed region (between 675 and 980 W $m^{-2}$ at 1300 UTC). These variations are due to the spatial distribution of cloud cover, which partially blocks incoming shortwave radiation in the nonwake region relative to the cloud free sheltered region. On the other hand, the longwave radiation has lower values (less cooling) in the sheltered (wake) region (~380 W $m^{-2}$) relative to the exposed (nonwake) area (~420 W $m^{-2}$).

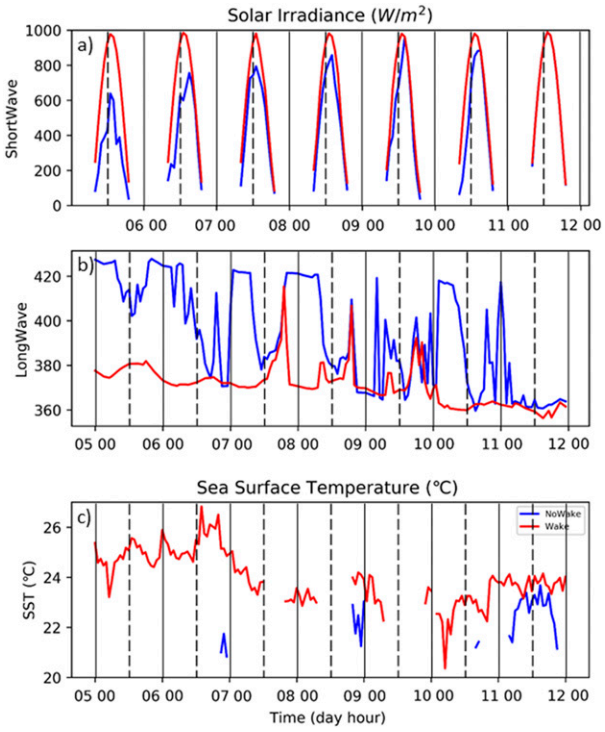


FIG. 3. EUMETSAT–*Meteosat-8* hourly data of surface downwelling (a) shortwave and (b) longwave radiation (W $m^{-2}$). (c) SST (°C) hourly oscillations at the exposed (blue line) and sheltered (red line) area, from 5 to 11 Aug 2017. The solid and dashed vertical lines represent 0000 and 1200 UTC, respectively, each day.

The SST was represented for the same study period (Fig. 3c). Therefore, the greater availability of surface data in the wake is due to the cloud-free conditions. Daily SST oscillations show temperature gradients reaching 2°C, when comparing sheltered and exposed regions (e.g., 6 August). There is a decrease of the SST during the first hours of the day (about 1°–2°C) and an increase during sunny hours (more than 2°C; 6 August), shown in Fig. 3c. When there are data available for the

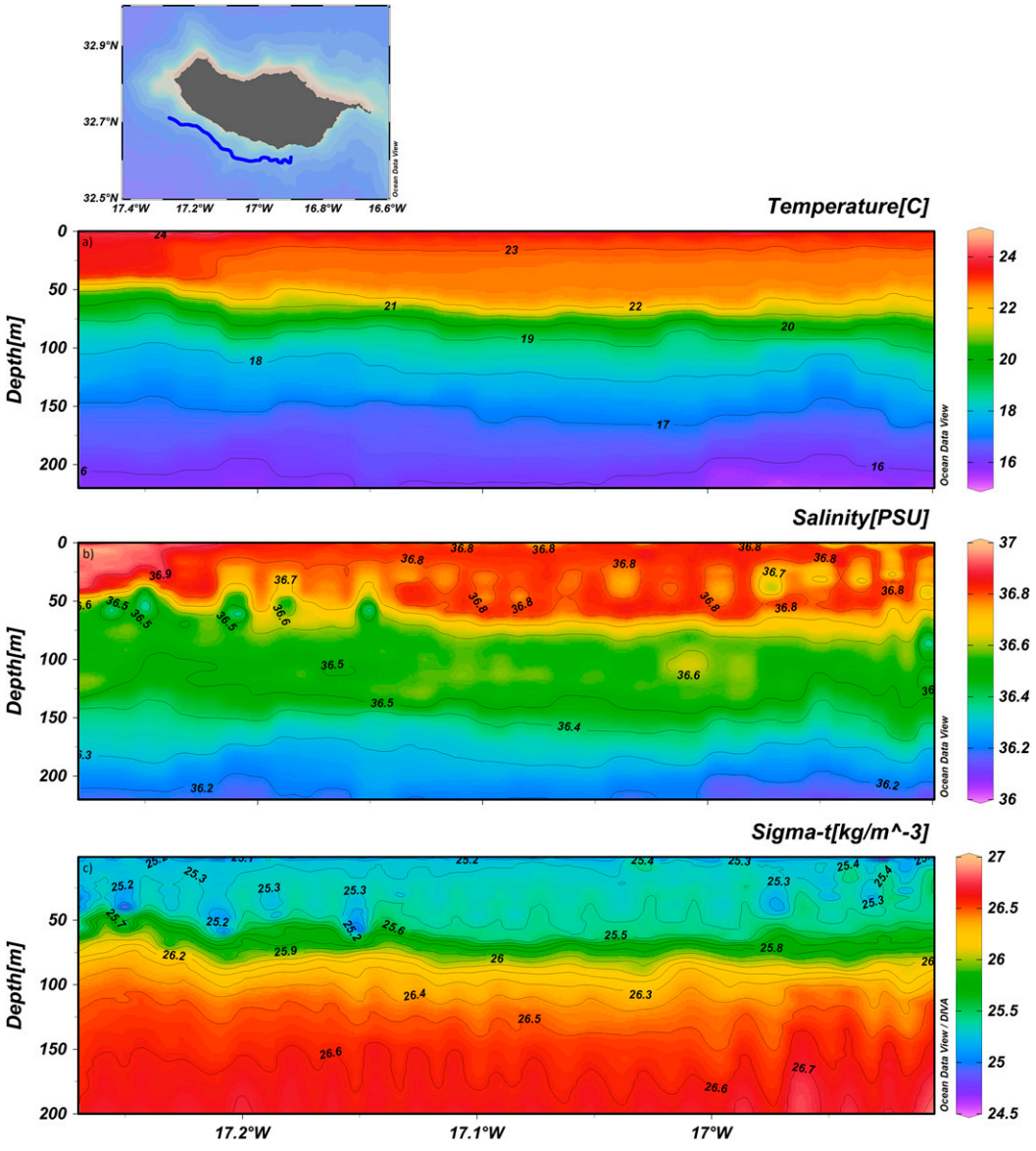


FIG. 4. Data collected using the uCTD during the Observatório Oceânico da Madeira 2017 (OOM 2017) expedition. (top) The transect (represented with a blue line) on the lee side of the island, in the sheltered area. (a) Temperature (°C), (b) salinity (psu), and (c) calculated density (sigma–theta; kg $m^{-3}$).

nonwake zone it is also possible to identify the ocean response vis-à-vis SST (e.g., 11 August; Fig. 3c), to the increase in available radiation (e.g., 11 August; Figs. 3a,b). Thus, a possible follow up question could be: What is the impact of the daily variation in solar irradiance and subsequent heating/cooling of the sea surface on the vertical structure of the water column, particularly in the leeward (wake) side of the island?

### *b. Vertical structure of water column in a leeward (wake) region*

To study how the atmospheric wake impacts the vertical structure of the water column, transect (Fig. 4) and vertical profiles (Fig. 5) were considered, for both the exposed and protected (wake) sides of the island (as shown in Fig. 1). The impact of intense solar radiation (Fig. 3) is noticeable in the vertical structure of the hydrographic section taken in the lee, particularly at the 1000-m isobath (Fig. 1, blue line). Note that these vertical cuts (Fig. 4) are a synoptic snapshot. While the vertical profiles of Fig. 5 have the advantage of showing the time variability of the measurements, the hydrographic section of Fig. 4 shows the spatial extent of these features.

In general, the water column was stratified, with higher temperature at the surface decreasing with depth (Fig. 4a). These values range from 24°C at the surface to 16°C at 200-m depth. A warmer (23.5°–24°C; Fig. 4a) and more saline (~37; Fig. 4b) water mass is depicted in the westernmost part of the

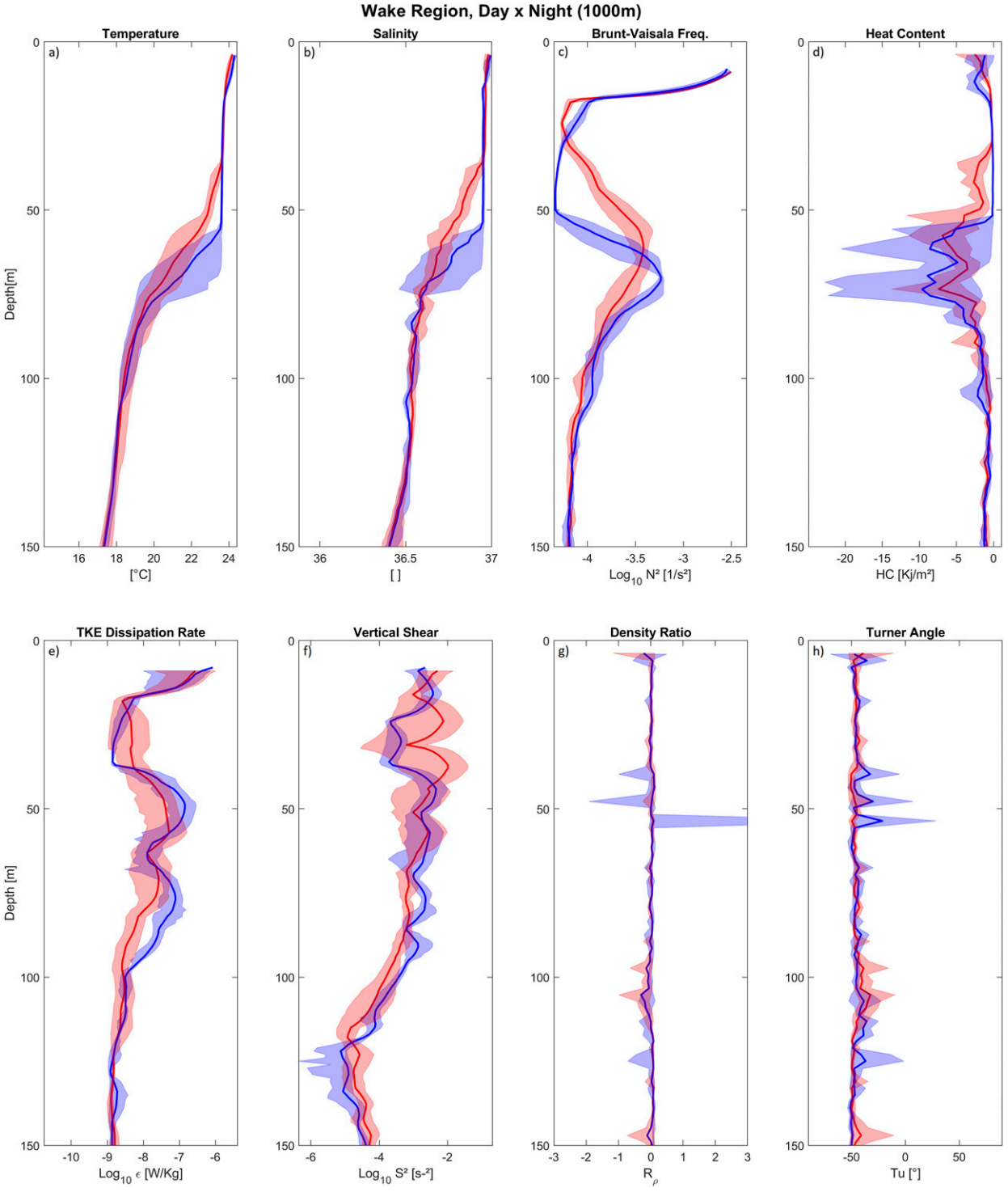


FIG. 5. Vertical profiles of the time-averaged (a) temperature (°C), (b) salinity (psu), (c) squared Brunt–Väisälä frequency ($s^{-2}$), (d) heat content ($kJ\,m^{-2}$), (e) turbulence kinetic energy (TKE; $W\,kg^{-1}$) dissipation rate, (f) vertical shear ($s^{-2}$), (g) density ratio, and (h) Turner angle (°) for daytime (red, stations Wd and Ed) and nighttime (blue, stations Wn and En) for the sheltered regions. (i)–(p) As in (a)–(h), but for the exposed regions. Shaded areas denote the 95% confidence intervals calculated using the bootstrap method.

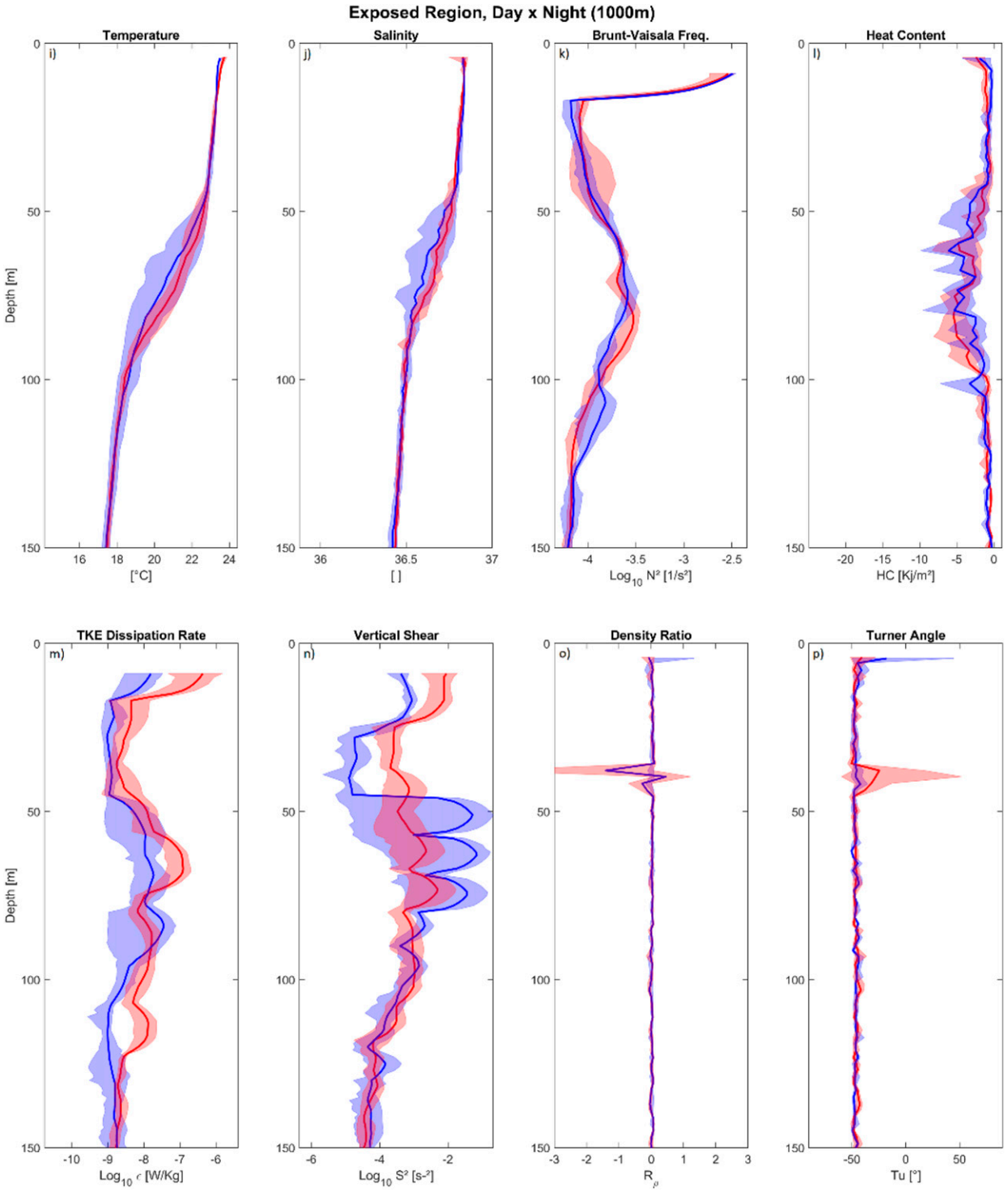


FIG. 5. (*Continued*)

transect, expanding down to 50-m depth, gradually fading away to the east. Furthermore, between the 50- and 70-m depth there is a greater proximity between isotherms (about 1°C per 5 m), representative of a well-defined thermocline. For the remaining of the transect, the temperature gradient varies approximately 1°C per 30 m of water. The presence of distinct water parcels with more/less salinity is also depicted in Fig. 4b. This brine water occurs throughout the whole transect, becoming more evident on the upper 60 m, on the western flank of the island. The seawater density (Fig. 4c)

has a similar behavior to the salinity. These dense water parcels occur in the first 50 m of water due to strong stratification.

To compare sheltered (wake) and exposed (nonwake) regions, four stations were sampled (X symbols shown in right panel of Fig. 1). Day and nighttime vertical profiles were also collected in sheltered (Wd and Wn) and in exposed regions (Ed and En; Fig. 5). Four profiles were taken in each station, except for Wd, which is represented by six profiles. The solid line (Fig. 5) represents the time-averaged profiles, and the shaded area represents the 95% confidence interval, calculated by the bootstrap method detailed above.

In contrast to the nonwake regions, there are noticeable differences between the day and night profiles in the wake. Temperature and salinity (Figs. 5a,b) decrease with depth, concurrently with an increase in potential density (Fig. S2 in the online supplemental material). The gradients in temperature and salinity profiles are smaller in the first ~35 m (about 0.017°C and 0.003 $m^{-1}$) during the day. During nighttime, these gradients extend to ~54-m depth (varying around 0.014°C and 0.001 $m^{-1}$). Note also that as a result of the daily variation in temperature the highest variability occurs within the thermocline, during nighttime. Furthermore, the largest daily loss of heat content occurs in the sheltered (wake) region (Figs. 5d,l). In the upper 12-m layer, values of ~|1.4| kJ $m^{-2}$ during the day decrease to ~|1| kJ $m^{-2}$ during nighttime. The vertical extension of the diurnal thermocline is marked by the increase of ~|2| kJ $m^{-2}$ on the night profile, at around 12-m depth. The strongest stratification of the water column, shown by the squared Brunt–Väisälä frequency (Fig. 5c), was measured at ~62-m depth during the day and at 70 m during the night, as a response to the nighttime expansion of the mixed layer depth (MLD). The sheltered region profiles are characterized by doubly stable layer, with $R_\rho \approx 0$ and Tu $\approx -45°$ both during day and night (Figs. 5g,h), and only a strong peak ($R_\rho > 3$), during nighttime.

The measured turbulence and shear profiles (Figs. 5e,f) corroborate this pattern. The turbulent kinetic energy rates are in general low, as expected for oceanic regions. Whereas for the sheltered region, the highest dissipation values occurred at night, coincident with the $R_\rho$ peak. In the first 15 m, the vertical shear was higher during the day, due to the stronger stratification of the surface layer.

While the day-and-night patterns can be distinguished in the sheltered region, in the exposed region profiles show similar behavior for day and nighttime. The night profile of vertical turbulence (Fig. 5m) does not show any distinct peaks bracing the thermocline. At night, the vertical shear (Fig. 5n) had a larger variation across the thermocline; however, this shear was not translated into the generation of a perceivable increase in turbulent dissipation. For temperature and salinity (Figs. 5i,j), an identical (night–day) behavior is observed. Although, both temperature and salinity decrease with depth, only in the thermocline zone there is a perceptible difference of values between the two periods. Nighttime cooling lowers the values of both temperature and salinity, since the ocean loses heat to the lower atmosphere during this period. The squared Brunt–Väisälä frequency profiles (Fig. 5k) show a reduction of stability ($d\rho/dz < 0$) in the first ~20 m, concurrent for day and night. These surface values can be related to the unstable stratification induced by the salinity. The Brunt–Väisälä frequency peaks between 50- and 1000-m depth, concurrent with the thermocline and halocline. The day-and-night similarities in the exposed (nonwake) region becomes even more evident on the profiles of density ratio (Fig. 5o) and Turner angle (Fig. 5p), where $R_\rho \approx 0$ and Tu $\approx -45°$. Although salt-fingering event is unlikely to occur under these physical conditions, the confidence interval does suggest a possibility of such an event to develop during daytime, particularly at 39.7 m ($R_\rho$ = 1.2; Tu = 52.1).

Resolving the upper-ocean diurnal variability can have important consequences for SST evolution on longer time scales (Bernie et al. 2005; Mujumdar et al. 2011). The heating of the sea surface takes place throughout the day, leading to evaporation and heat transfer to the lower atmosphere at night. As this is a cumulative process, understanding how it progresses over time become one of the main objectives of this work. The data collected with the Wirewalker, on 23 and 24 July 2018, provide a space–temporal evolution of the water column within the wake (Fig. 1). During July 2018, as in August 2017, the wake of warm-water wake was visible, with sea surface temperatures close to 23.5°C. The Wirewalker measurements (Fig. 6a) show that the temperature in the water column decreased with depth, reaching a minimum value of ~18°C. The temperature gradient is greater in the first 20 m and, once again, near the coast due to vertical mixing processes at the insular shelf edge. Figure 6b shows the salinity values with density (sigma–theta) contours, along the transect varying with depth. Although the water column appears vertically stratified, parcels of high salinity are scattered throughout surface. The contours of density show a surface gradient with values varying between 25.3 and 26.5 kg $m^{-3}$.

The hourly profiles of temperature collected with the Wirewalker in the warm-wake region are represented in Fig. 7. The response of the mixed layer to the incident solar radiation is clear. During the sunny hours, just after the peak of shortwave radiation (~1300 UTC), the mixed layer stretches to deeper layers (~20–45 m). At the surface, the vertical profiles showed a significant variation (expansion and contraction) of the daily thermocline.

### c. *Model results*

The coupled numerical model represented the formation of the warm wake in the leeward side of the island. The panels of Fig. 8 show a snapshot of wind (Fig. 8a), cloud cover (Fig. 8b), total radiation (net shortwave + net longwave + latent heat + sensible heat; Fig. 8c) and SST (Fig. 8d). As observed, during this particular warm wake event, the wind was predominantly from North quadrant with average speeds oscillating from 6 to 8 m $s^{-1}$, reaching almost zero in the wake region, forming jets with ~12 m $s^{-1}$ on the flanks of the island. It is also perceptible the change in the wind direction on the southwest side. Simultaneously, Fig. 8b, shows the absence of the cloud cover in the leeward side, when compared to the oceanic surroundings. For total radiation escaping from the ocean (Fig. 8c), the values are small in the wake area, relative to the flanks and to the windward side (~650 and ~820 W $m^{-2}$, respectively).

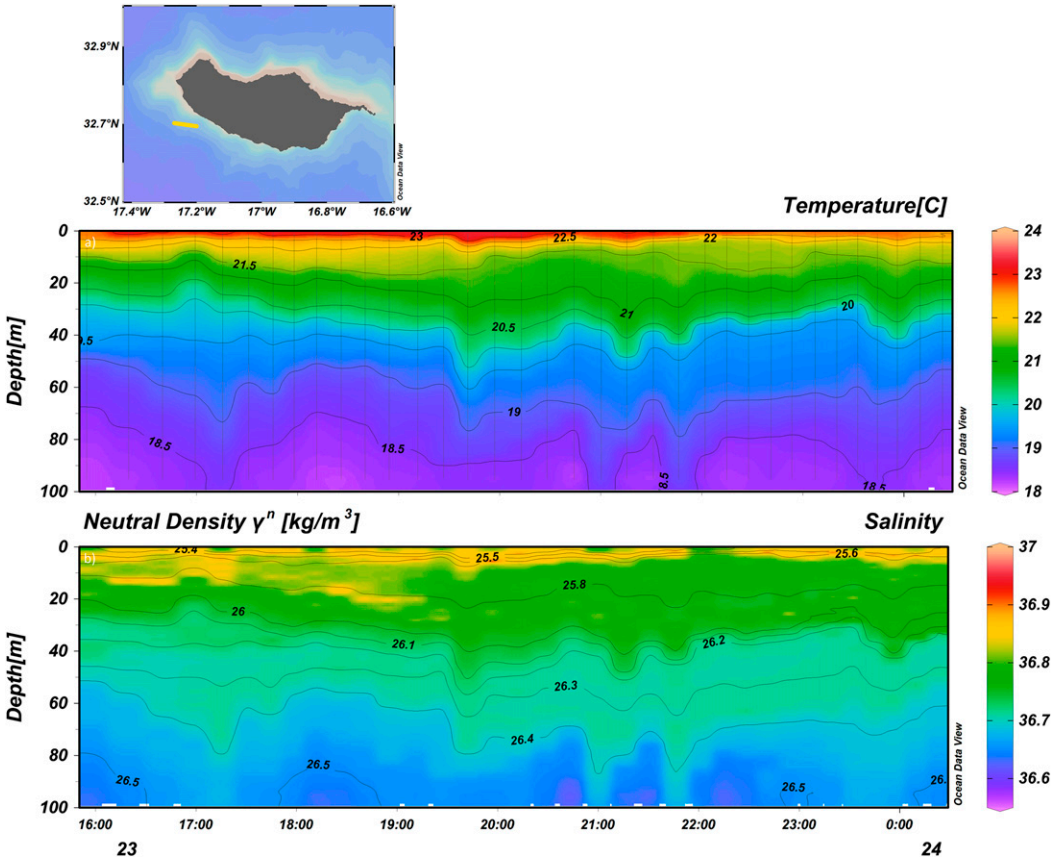


FIG. 6. Wirewalker data, collected in July 2018 in the Madeira warm-wake region for (a) temperature (°C) and (b) salinity (psu) (colors), along with neutral density (kg m$^{-3}$; contours). (top) The sampling area, represented by the yellow line.

The values of SST (Fig. 8d) are representative of warm water generation in the wake with values of ~25°C, and (close to) 26°C near to the coast. The offshore oceanic conditions show colder temperatures (between 22° and 24°C), including the formation of mesoscale features, such as an eddy generated between Madeira and Desertas Islands, inducing horizontal mixing and thus contributing to rapid cooling of the surface waters on the eastern side of the island.

Figure 9 shows the model section representing the transect of Fig. 1 (1000-m bathymetric, parallel to the coast). Figures 9a and 9b shows the temperature and the MLD (black line; computation of the MLD considered $|\Delta\rho| < \pm 0.3$ kg m$^{-3}$; the threshold was determined using historical oceanic profiles near Madeira), for night and daytime, respectively. As expected, the temperature values at the surface are higher during the day (>24°C), and the MLD is located between 4 and 16 m (Fig. 9b). During nighttime (Fig. 9a), the temperature values at the surface are cooler, close to 23°C, and the MLD sinks to 30–38 m. These patterns are in line with the measurements obtained with the CTD (Fig. 5) and with the Wirewalker (Figs. 6 and 7), around Madeira. The model also represents the stable surface conditions during the day (Brunt–Väisälä frequency = $8 \times 10^{-4}$ s$^{-2}$, Fig. 9f), corroborated by the occurrence of daily thermoclines at the surface (Fig. 9b). Between 30- and 50-m depth, there are also large values of stability (Brunt–Väisälä frequency = $3.4 \times 10^{-4}$ s$^{-2}$, Fig. 9f), concurrent with higher shear on the MLD. The values of salinity for night and daytime are represented in Figs. 9c and 9d, respectively. Although spatial resolution of COAWST is lower than the observations, saline convection has been (partially) resolved by the model. It is possible to identify the sinking of surface water parcels with high salinity to deeper layers (17.268°W at 80 m). The differences between night and day, however, are not well resolved by the model.

## 5. Summary and discussion

Most of the scientific literature on salt-fingering/diffusive convection has been carried out in laboratories and/or using numerical model simulations (e.g., Schmitt 2003; Yang et al. 2016; Rehman and Singh 2017). Most observational studies are focused on enclosed seas, lakes, and lagoons (e.g., Zodiatis and Gasparini 1996; Shi and Wei 2007; Pérez-Santos et al. 2014; Arnon et al. 2016), and a few authors measured convection in large-scale oceanic conditions (e.g., Schmitt 1981, 2003; Holbrook et al. 2003; Nagai et al. 2015).

In this study, local observations show that island wakes induce saline convection in open ocean conditions over a 24-h period. Gentemann et al. (2003) characterized the distribution

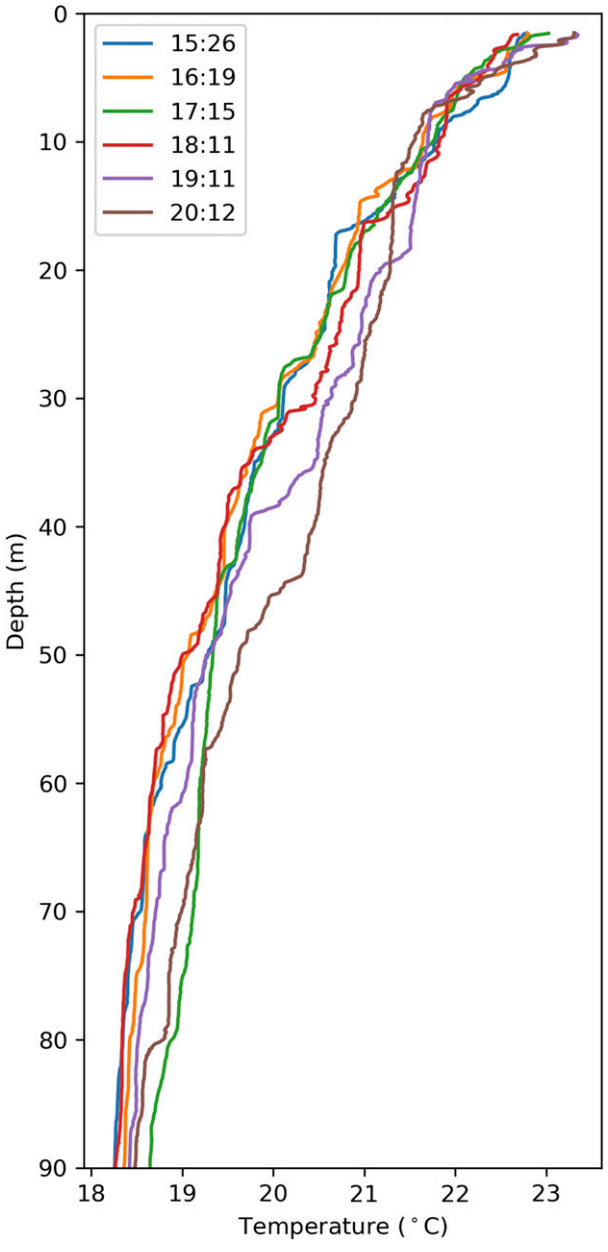


FIG. 7. Hourly vertical profiles of temperature (°C), extracted from the Wirewalker (upcasts only), between 1526 and 2012 UTC 23 Jul 2018 while the instrument was drifting in the wake region.

of SST diurnal warming in oceanic regions, showing that in summertime this warming is responsible for the diurnal stratification in the mid–North Atlantic, and estimated that, for instantaneous wind speeds of less than 1 m s$^{-1}$, diurnal warming events that are larger than 5°C occur 0.5% of the time. The 2°C in diurnal SST can contribute to establish a significant temperature gradient, as observed in the warm wake region; thus, the role of convection processes in the North Atlantic might be underestimated.

The stability properties of the local stratification are defined by the $R_\rho$ (Ruddick 1983), which helped us to identify the distinct water parcels as salt fingers (Fig. 5g). The $R_\rho$ measures the degree of compensation between temperature and salinity gradients in terms of their effects on density stratification. Thus, large values of $R_\rho$ imply that density distribution is controlled by thermal components (Radko 2013). Hage and Tilgner (2010) have reported, using an electrochemical technique, that salt-finger convection can occur even for $10^{-2} < R_\rho < 1$. In fact, according to Rehman and Singh (2017), in oceanic conditions most of the salt fingers form at low $R_\rho$ ($R_\rho \rightarrow 1$). Schmitt (1981) affirms that the largest temperature range appears to be a better fit for lower $R_\rho$, where we expect salt fingering to make a stronger contribution to the mixing processes. In addition, Schmitt (2003) restates that the propensity toward salt-fingering formation is a function of the unstable vertical salinity gradient in response to high evaporation rates, as it is the case in the wake of Madeira.

The formation of the Madeira wakes has been discussed by several authors (Caldeira et al. 2002; Grubišić et al. 2015; Pullen et al. 2017b). The increase of the SST and subsequent stratification of the water column (warm oceanic wake) are direct consequences of the atmospheric wake. As the SST warming is a cumulative process, the evaporation/cooling of the surface may trigger the salinity instability. Alexander et al. (2000) studied the variability of the upper ocean in the Northern Hemisphere in terms of SST and MLD. The authors suggested that anomalies in the net heat flux, MLD, and entrainment heat flux provided a significant contribution to the growth of SST anomalies. During summer, most of the heat flux across the base of the mixed layer is associated with mixing in a convectively stable environment. In our study, the variability of MLD during day/night induces sinking of the mixed layer (Fig. 7), confirming the relation between heat flux, SST and MLD. Besides the variability of the MLD, the thermocline structure seems to change during day/nighttime. It is clearly visible (Figs. 5a,b) the increased of the thermocline's sharp gradient during nighttime. Arnon et al. (2016), studied the thermohaline stratification in a Dead Sea, in salt-finger conditions, fluxes transport heat and salt away from the interface resulting in a sharpened interface over time. The interface sharpening is a consequence of staircase formation, which is also noted in the Madeira profiles as shown in Fig. 7.

Arnon et al. (2016) considered two major atmospheric forcing mechanisms: (i) the stratigraphic dynamics of a hypersaline lake, characterized by a continuous negative water balance that increases superficial layer salinity, and (ii) the seasonal heat inputs, which govern the seasonal thermal stratification. In the present warm wake (summer) study, however, solar radiation governs thermal stratification and the absence of winds plays an important role preventing mixing at the sea surface. Boehrer and Schultze (2008) showed that in deep lakes, during the summer, once stratification is established, surface layers become thermally and chemically distinct from deeper water layers (permeability theory), which is clearly not the case in open-ocean conditions. In addition, Stern (1960) affirmed that in oceans, stratification can actually be dynamically unstable, due to greater diffusivity of heat relative to salt, leading to convection. Our study does shows that the high surface salinity values in the wake region

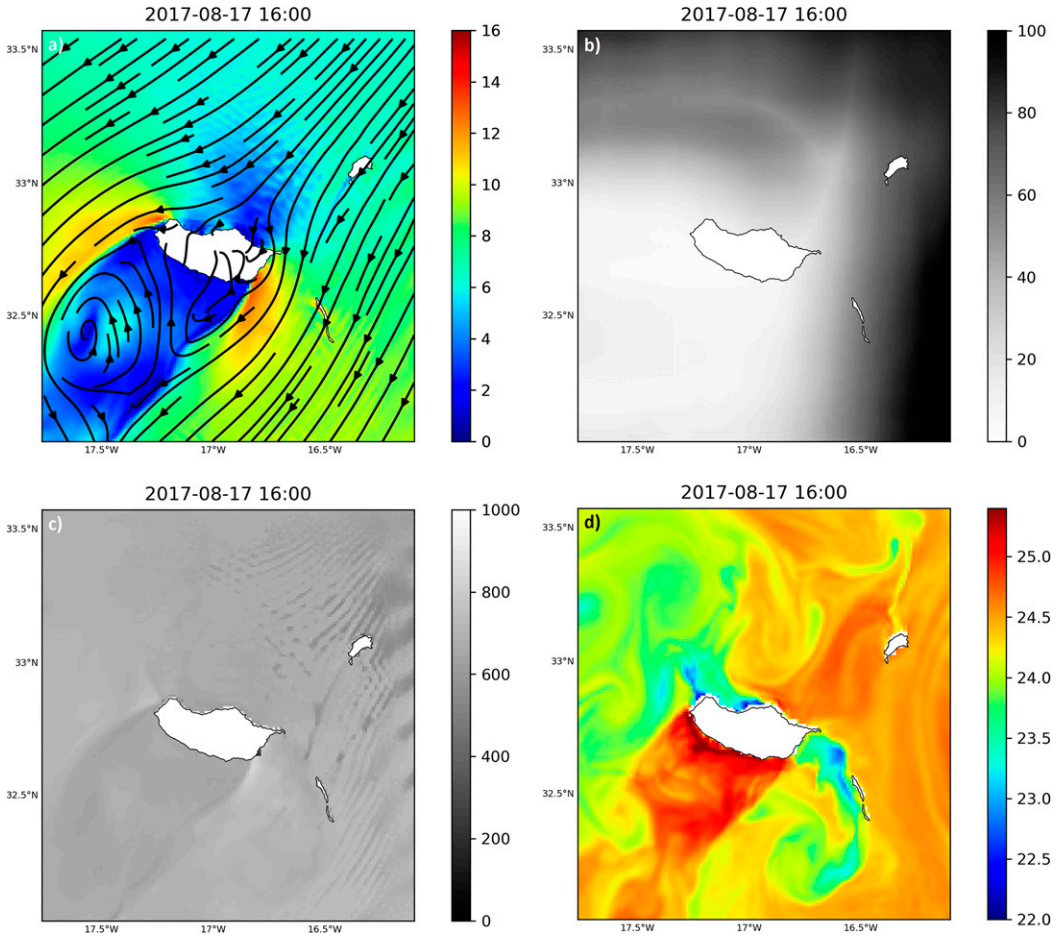


FIG. 8. The 16 and 17 August 2017 COAWST model results for (a) wind speed ($m\,s^{-1}$; colors) and wind direction (streamlines), (b) cloud cover (%), (c) total radiation ($W\,m^{-2}$), and (d) SST (°C).

destabilizes the stratified layer, inducing a cascade of saline waters mass to deeper layers, in line with Stern (1960). The daily heating cycle generates a strong temperature gradient in the water column; however, the instability can be subsequently fueled by evaporation and overnight cooling of the sea surface (in the absence of solar radiation and thus heat source). We believe that the stretching of the mixed layer is a consequence of the change in density properties at the ocean surface, accountable for the loss of heat to the atmosphere and consequent weakening of stratification, thus enabling the nighttime vertical excursions of salt parcels. As depicted in Fig. 7, during the day, the stretching of the mixed layer begins after the peak of solar radiation, most likely due to the loss of heat by evaporation. During the night, however, this loss of heat (by cooling) and consequently deepening of the mixed layer (showed in Figs. 5b and 9a) can also be a response to the intensification of the wind (Bourassa et al. 2010). The mean of simulated meridional wind for the wake region at 13 m of altitude is represented in Fig. 10, for the first hours of the day (9 h; Fig. 10a) and night (21 h; Fig. 10b). Sea and mountain breezes are a response to the temperature gradients between the land and the sea; therefore, sunrise and sunset are two key moments for their formation. Comparing with daytime, the intensification of the meridional (down valley) winds after sunset (Fig. 10b), despite only measuring $\sim 2\,m\,s^{-1}$, can also contribute for the deepening the mixed layer, as shown previously.

Some authors have represented some of the atmospheric–oceanic processes in the region of Madeira Island through numerical models. Couvelard et al. (2012) focused on the wind-mediated vorticity generation and eddy confinement. The surface signature of the warm water wake was previously represented numerically, without observations, nor detailed discussion on its effects in the water column (Pullen et al. 2017a,b). Representing the saline convection, in this study, was a challenge, considering that the model resolution (1 km) was coarse to adequately represent the sinking of the MLD as observed during in situ campaigns reported here. Future efforts should consider measurements of thermocline dynamics for longer periods, as well as relying on nonhydrostatic modeling to study the nighttime convective processes. Ouillon et al. (2019) used a two-dimensional numerical approach to study the role of salt-fingering formation in the metalimnion of a hypersaline lake (the Dead Sea). In our case, we used a 3D fully hydrostatic oceanic circulation model, coupled with a 3D

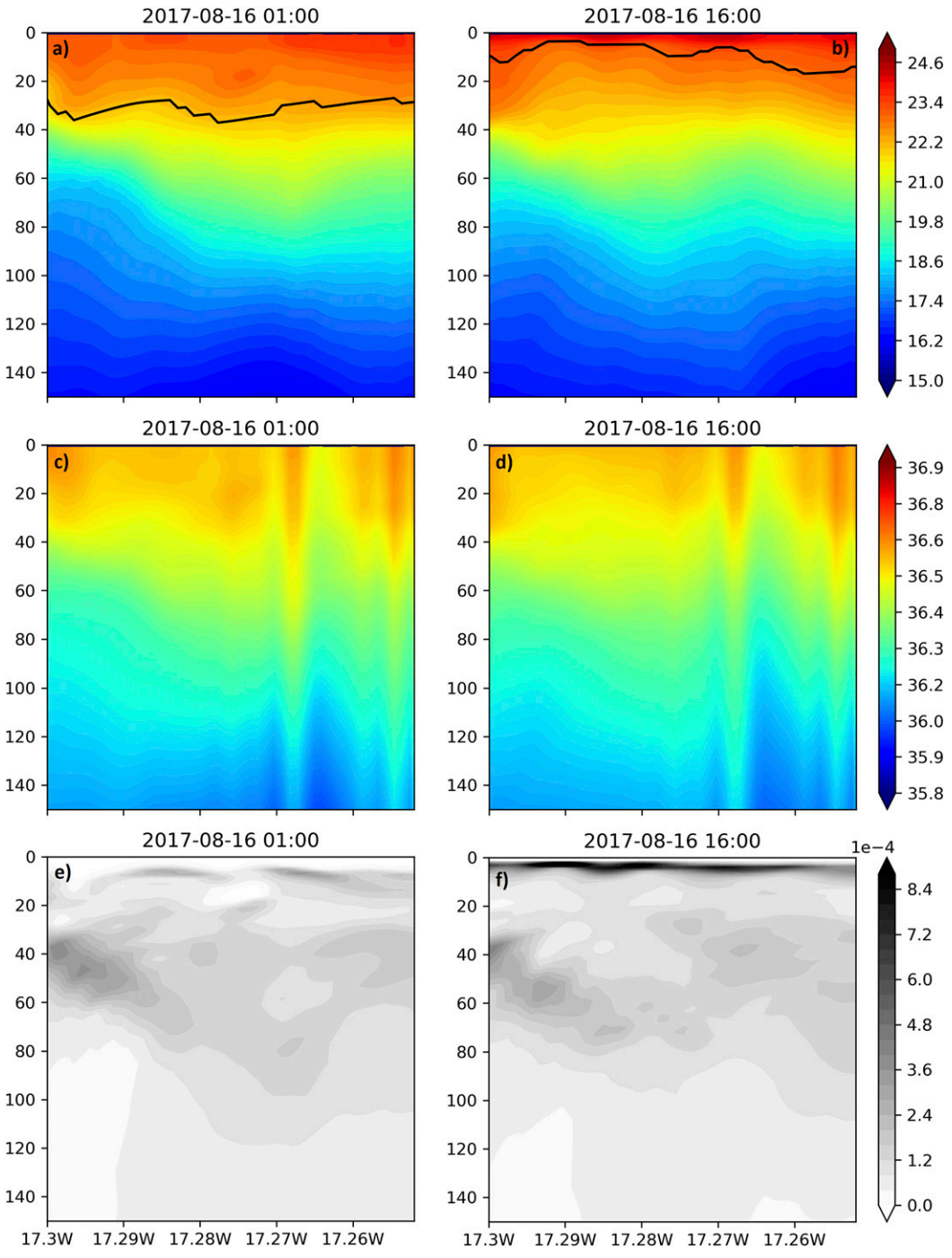


FIG. 9. Vertical section corresponding to the transect represented in Fig. 1, for (left) nighttime and (right) daytime for (a),(b) temperature (°C; colors) and mixed layer depth (black line; m); (c),(d) salinity (psu); and (e),(f) squared Brunt–Väisälä frequency ($s^{-2}$).

nonhydrostatic meteorological model, to best represent the observable conditions around the island. To the best of our knowledge, no prior study attempted to resolve these complex upper oceanic conditions using coupled models. Nevertheless, our simulation does not consider convection effects. However, the GLS surface mixed layer scheme, recently referred as an accurate scheme by Damerell et al. (2020), is capable of (partially) simulating the warm/saltwater sinking, particularly in the wake, suggesting that, apart from the thermodynamic convection forcing, other energetic processes such as shear

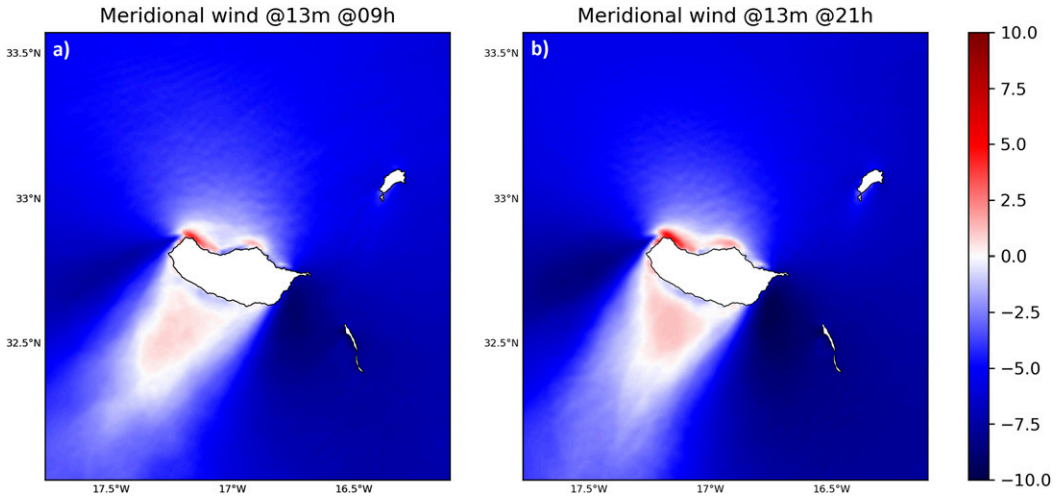


FIG. 10. August mean meridional wind component ($m\,s^{-1}$), at 13 m of altitude, simulated by COAWST for (a) 0900 UTC and (b) 2100 UTC.

instabilities and/or internal waves might be contributing to the vertical mixing.

The study of these local phenomena can provide valuable insights into the study of Earth's climate. Xie et al. (2001) reported that in the tropics, interactions between wind, evaporation and SST provides a positive feedback, and therefore, shape the spatial and temporal variability of the regional climate. Thus, the findings of our work can be expanded in future research to link, the atmosphere and the deep ocean, in particularly with regard to the impacts on chemical distribution (e.g., carbon transport), nutrient distribution (i.e., downwelling processes), and biological production (e.g., marine snow). In fact, Radko (2013) states that this kind of convection (salt finger/diffuse) contributes to the vertical transport of heat and carbon dioxide through the thermocline, affecting air–sea fluxes and thereby impacting the global climate—thus requiring further research.

*Acknowledgments.* We acknowledge the captain and crew of R/V *SOCIB* and of R/V *NRP Gago Coutinho* for their professionalism and cooperation during data collection. For Mission Structure for the Extension of the Continental Shelf (EMPEC), Bruno Ramos is acknowledged for the operation of the uCTD. We also thank João Vitorino (from the Hydrographic Institute of the Portuguese Navy), Cláudio Cardoso, and Jesus Reis (from the Oceanic Observatory of Madeira) for constructive discussions on the subject. Comments from an anonymous reviewer have substantially improved the first version of this paper. This work was financially supported by the Oceanic Observatory of Madeira Project (M1420-01-0145- FEDER-000001-Observatório Oceânico da Madeira-OOM). Author C. C. Azevedo is currently funded by FCT (SFRH/BD/147425/2019).

*Data availability statement.* Because of the proprietary nature of some of the data used in this study, access is restricted. Contact catia.azevedo@oom.arditi.pt for complete access and usage of the dataset.

## REFERENCES

Alexander, M. A., J. D. Scott, and C. Deser, 2000: Processes that influence sea surface temperature and ocean mixed layer depth variability in a coupled model. *J. Geophys. Res.*, **105**, 16 823–16 842, https://doi.org/10.1029/2000JC900074.

Alves, J. M. R., R. M. A. Caldeira, and P. M. A. Miranda, 2020: Dynamics and oceanic response of the Madeira tip-jets. *Quart. J. Roy. Meteor. Soc.*, **146**, 3048–3063, https://doi.org/10.1002/qj.3825.

Arnon, A., J. S. Selker, and N. G. Lensky, 2016: Thermohaline stratification and double diffusion diapycnal fluxes in the hypersaline Dead Sea. *Limnol. Oceanogr.*, **61**, 1214–1231, https://doi.org/10.1002/lno.10285.

Bernie, D. J., S. J. Woolnough, J. M. Slingo, and E. Guilyardi, 2005: Modeling diurnal and intraseasonal variability of the ocean mixed layer. *J. Climate*, **18**, 1190–1202, https://doi.org/10.1175/JCLI3319.1.

Boehrer, B., and M. Schultze, 2008: Stratification of lakes. *Rev. Geophys.*, **46**, RG2005, https://doi.org/10.1029/2006RG000210.

Bourassa, M., S. Gille, D. Jackson, J. B. Roberts, and G. Wick, 2010: Ocean winds and turbulent air-sea fluxes inferred from remote sensing. *Oceanography*, **23**, 36–51, https://doi.org/10.5670/oceanog.2010.04.

Caldeira, R. M. A., and P. Sangrà, 2012: Complex geophysical wake flows. *Ocean Dyn.*, **62**, 683–700, https://doi.org/10.1007/s10236-012-0528-6.

——, and R. Tomé, 2013: Wake response to an ocean-feedback mechanism: Madeira Island case study. *Bound.-Layer Meteor.*, **148**, 419–436, https://doi.org/10.1007/s10546-013-9817-y.

——, S. Groom, P. Miller, D. Pilgrim, and N. P. Nezlin, 2002: Sea-surface signatures of the island mass effect phenomena around Madeira Island, Northeast Atlantic. *Remote Sens. Environ.*, **80**, 336–360, https://doi.org/10.1016/S0034-4257(01)00316-9.

——, A. Stegner, X. Couvelard, I. B. Araújo, P. Testor, and A. Lorenzo, 2014: Evolution of an oceanic anticyclone in the lee of Madeira Island: In situ and remote sensing survey. *J. Geophys. Res. Oceans*, **119**, 1195–1216, https://doi.org/10.1002/2013JC009493.

——, X. Couvelard, R. Vieira, C. Lucas, I. Sala, and I. Vallès Casanova, 2016: Challenges of building an operational ocean forecasting system for small island regions: Regional to local. *J. Oper. Oceanogr.*, **9**, 1–12, https://doi.org/10.1080/1755876X.2016.1205304.

Chapman, D. C., 1985: Numerical treatment of cross-shelf open boundaries in a barotropic coastal ocean model. *J. Phys. Oceanogr.*, **15**, 1060–1075, https://doi.org/10.1175/1520-0485(1985)015<1060:NTOCSO>2.0.CO;2.

Copernicus Climate Change Service, 2017: ERA5: Fifth generation of ECMWF atmospheric reanalyses of the global climate. Copernicus Climate Change Service Climate Data Store, https://cds.climate.copernicus.eu/cdsapp#!/home.

Couvelard, X., R. M. A. Caldeira, I. B. Araújo, and R. Tomé, 2012: Wind mediated vorticity-generation and eddy-confinement, leeward of the Madeira Island: 2008 numerical case study. *Dyn. Atmos. Oceans*, **58**, 128–149, https://doi.org/10.1016/j.dynatmoce.2012.09.005.

Damerell, G. M., K. J. Heywood, D. Calvert, A. L. M. Grant, M. J. Bell, and S. E. Belcher, 2020: A comparison of five surface mixed layer models with a year of observations in the North Atlantic. *Prog. Oceanogr.*, **187**, 102316, https://doi.org/10.1016/j.pocean.2020.102316.

Dong, C., and J. C. McWilliams, 2007: A numerical study of island wakes in the Southern California Bight. *Cont. Shelf Res.*, **27**, 1233–1248, https://doi.org/10.1016/j.csr.2007.01.016.

Dudhia, J., 1989: Numerical study of convection observed during the winter monsoon experiment using a mesoscale two-dimensional model. *J. Atmos. Sci.*, **46**, 3077–3107, https://doi.org/10.1175/1520-0469(1989)046<3077:NSOCOD>2.0.CO;2.

Efron, B., and G. Gong, 1983: A leisurely look at the bootstrap, the jackknife, and cross-validation. *Amer. Stat.*, **37**, 36–48, https://doi.org/10.1080/00031305.1983.10483087.

Galperin, B., S. Sukoriansky, and P. S. Anderson, 2007: On the critical Richardson number in stably stratified turbulence. *Atmos. Sci. Lett.*, **8**, 65–69, https://doi.org/10.1002/asl.153.

Gentemann, C. L., C. J. Donlon, A. Stuart-Menteth, and F. J. Wentz 2003: Diurnal signals in satellite sea surface temperature measurements. *Geophys. Res. Lett.*, **30**, 1140, https://doi.org/10.1029/2002GL016291.

Godøy, Ø., 2016: Operational high latitude surface irradiance products from polar orbiting satellites. *Polar Sci.*, **10**, 564–575, https://doi.org/10.1016/j.polar.2016.10.001.

Grubišić, V., J. Sachsperger, and R. M. A. Caldeira, 2015: Atmospheric wake of Madeira: First aerial observations and numerical simulations. *J. Atmos. Sci.*, **72**, 4755–4776, https://doi.org/10.1175/JAS-D-14-0251.1.

Hage, E., and A. Tilgner, 2010: High Rayleigh number convection with double diffusive fingers. *Phys. Fluids*, **22**, 076603, https://doi.org/10.1063/1.3464158.

Haidvogel, D. B., and A. Beckmann, 1999: *Numerical Ocean Circulation Modelling*. Imperial College Press, 344 pp.

Holbrook, W. S., P. Páramo, S. Pearse, and R. W. Schmitt, 2003: Thermohaline fine structure in an oceanographic front from seismic reflection profiling. *Science*, **301**, 821–824, https://doi.org/10.1126/science.1085116.

Hong, S.-Y., J. Dudhia, and S.-H. Chen, 2004: A revised approach to Ice microphysical processes for the bulk parameterization of clouds and precipitation. *Mon. Wea. Rev.*, **132**, 103–120, https://doi.org/10.1175/1520-0493(2004)132<0103:ARATIM>2.0.CO;2.

Hubert, L. F., and A. F. Krueger, 1962: Satellite pictures of mesoscale eddies. *Mon. Wea. Rev.*, **90**, 457–463, https://doi.org/10.1175/1520-0493(1962)090<0457:SPOME>2.0.CO;2.

Itoh, S., I. Yasuda, T. Nakatsuka, J. Nishioka, and Y. N. Volkov, 2010: Fine- and microstructure observations in the Urup Strait, Kuril Islands, during August 2006. *J. Geophys. Res.*, **115**, C08004, https://doi.org/10.1029/2009JC005629.

Janjić, Z. I., 1990: The step-mountain coordinate: Physical package. *Mon. Wea. Rev.*, **118**, 1429–1443, https://doi.org/10.1175/1520-0493(1990)118<1429:TSMCPP>2.0.CO;2.

——, 1994: The step-mountain Eta coordinate model: Further developments of the convection, viscous sublayer, and turbulence closure schemes. *Mon. Wea. Rev.*, **122**, 927–945, https://doi.org/10.1175/1520-0493(1994)122<0927:TSMECM>2.0.CO;2.

——, 1996: The surface layer in the NCEP Eta Model. *Proc. 11th Conf. on Numerical Weather Prediction*, Norfolk, VA, Amer. Meteor. Soc., 354–355.

——, 2002: Nonsingular implementation of the Mellor-Yamada level 2.5 scheme in the NCEP meso model. NCEP Office Note 437, 61 pp., http://www.emc.ncep.noaa.gov/officenotes/newernotes/on437.pdf.

Kantha, L., and C. Clayson, 2002: Double-diffusive processes. *Small Scale Processes in Geophysical Fluid Flows*, International Geophysics Series, Vol. 67, Academic Press, 685–733, https://doi.org/10.1016/S0074-6142(00)80083-2.

Lueck, R., 2016: Calculating the rate of dissipation of turbulent kinetic energy. RSI Tech. Note 028, 18 pp., http://rocklandscientific.com/support/knowledge-base/technical-notes/.

——, and E. Murowinski, 2017: A guide to data processing. RSI Tech. Note 039, 53 pp., http://rocklandscientific.com/support/knowledge-base/technical-notes/.

Marchesiello, P., J. C. McWilliams, and A. Shchepetkin, 2001: Open boundary conditions for long-term integration of regional oceanic models. *Ocean Modell.*, **3**, 1–20, https://doi.org/10.1016/S1463-5003(00)00013-5.

Marsouin, A., 2017: Radiative fluxes over Indian Ocean from *METEOSAT-8* data, validation report. Météo-France/CMS Validation Rep. SAF/OSI/CDOP3/MF/SCI/RP/305, 4 pp., http://www.osi-saf.org/lml/doc/osisaf_cdop3_ss1_svr_meteosat08_io_flx.pdf.

Mason, E., J. Molemaker, A. F. Shchepetkin, F. Colas, J. C. McWilliams, and P. Sangrà, 2010: Procedures for offline grid nesting in regional ocean models. *Ocean Modell.*, **35**, 1–15, https://doi.org/10.1016/j.ocemod.2010.05.007.

Mensah, V., M. Le Menn, and Y. Morel, 2009: Thermal mass correction for the evaluation of salinity. *J. Atmos. Oceanic Technol.*, **26**, 665–672, https://doi.org/10.1175/2008JTECHO612.1.

——, F. Roquet, L. Siegelman-Charbit, B. Picard, E. Pauthenet, and C. Guinet, 2018: A correction for the thermal mass–induced errors of CTD tags mounted on marine mammals. *J. Atmos. Oceanic Technol.*, **35**, 1237–1252, https://doi.org/10.1175/JTECH-D-17-0141.1.

Minnett, P. J., and Coauthors, 2019: Half a century of satellite remote sensing of sea-surface temperature. *Remote Sens. Environ.*, **233**, 111366, https://doi.org/10.1016/j.rse.2019.111366.

Mlawer, E. J., S. J. Taubman, P. D. Brown, M. J. Iacono, and S. A. Clough, 1997: Radiative transfer for inhomogeneous atmospheres: RRTM, a validated correlated-*k* model for the longwave. *J. Geophys. Res.*, **102**, 16 663–16 682, https://doi.org/10.1029/97JD00237.

Mujumdar, M., K. Salunke, S. A. Rao, M. Ravichandran, and B. N. Goswami, 2011: Diurnal cycle induced amplification of sea surface temperature intraseasonal oscillations over the Bay of Bengal in summer monsoon season. *IEEE Geosci. Remote Sens. Lett.*, **8**, 206–210, https://doi.org/10.1109/LGRS.2010.2060183.

Na, H., K.-Y. Kim, K.-I. Chang, J. J. Park, K. Kim, and S. Minobe, 2012: Decadal variability of the upper ocean heat content in the East/Japan Sea and its possible relationship to northwestern

Pacific variability. *J. Geophys. Res.*, **117**, C02017, https://doi.org/10.1029/2011JC007369.

Nagai, T., R. Inoue, A. Tandon, and H. Yamazaki, 2015: Evidence of enhanced double-diffusive convection below the main stream of the Kuroshio Extension. *J. Geophys. Res. Oceans*, **120**, 8402–8421, https://doi.org/10.1002/2015JC011288.

Osborn, T. R., 1980: Estimates of the local rate of vertical diffusion from dissipation measurements. *J. Phys. Oceanogr.*, **10**, 83–89, https://doi.org/10.1175/1520-0485(1980)010<0083:EOTLRO>2.0.CO;2.

Ouillon, R., N. G. Lensky, V. Lyakhovsky, A. Arnon, and E. Meiburg, 2019: Halite precipitation from double-diffusive salt fingers in the Dead Sea: Numerical simulations. *Water Resour. Res.*, **55**, 4252–4265, https://doi.org/10.1029/2019WR024818.

Pérez-Santos, I., J. Garcés-Vargas, W. Schneider, L. Ross, S. Parra, and A. Valle-Levinson, 2014: Double-diffusive layering and mixing in Patagonian fjords. *Prog. Oceanogr.*, **129**, 35–49, https://doi.org/10.1016/j.pocean.2014.03.012.

Pinkel, R., M. A. Goldin, J. A. Smith, O. M. Sun, A. A. Aja, M. N. Bui, and T. Hughen, 2011: The Wirewalker: A vertically profiling instrument carrier powered by ocean waves. *J. Atmos. Oceanic Technol.*, **28**, 426–435, https://doi.org/10.1175/2010JTECHO805.1.

Pullen, J., and Coauthors, 2017a: Coupled ocean-atmosphere forecasting at short and medium time scales. *J. Mar. Res.*, **75**, 877–921, https://doi.org/10.1357/002224017823523991.

——, R. Caldeira, J. D. Doyle, P. May, and R. Tomé, 2017b: Modeling the air-sea feedback system of Madeira Island. *J. Adv. Model. Earth Syst.*, **9**, 1641–1664, https://doi.org/10.1002/2016MS000861.

Radko, T., 2013: *Double-Diffusive Convection*. Cambridge University Press, 342 pp.

Rehman, F., and O. P. Singh, 2017: Salt finger convection at marginal stability. *Geophys. Astrophys. Fluid Dyn.*, **111**, 323–332, https://doi.org/10.1080/03091929.2017.1356923.

Ruddick, B., 1983: A practical indicator of the stability of the water column to double-diffusive activity. *Deep-Sea Res.*, **30A**, 1105–1107, https://doi.org/10.1016/0198-0149(83)90063-8.

Saux Picart, S., A. Marsouin, and S. Péré, 2015: Validation report for OSI SAF Metop/AVHRR SST OSI-201b/OSI-202-b/OSI-204-b. Météo-France/CMS Validation Rep. SAF/OSI/CDOP2/M-F/SCI/TEC/234, 21 pp., http://www.osi-saf.org/lml/doc/osisaf_cdop2_ss1_sst_metop_validation_report.pdf.

Schmitt, R. W., 1981: Form of the temperature–salinity relationship in the central water: Evidence for double-diffusive mixing. *J. Phys. Oceanogr.*, **11**, 1015–1026, https://doi.org/10.1175/1520-0485(1981)011<1015:FOTTSR>2.0.CO;2.

——, 2003: Observational and laboratory insights into salt finger convection. *Prog. Oceanogr.*, **56**, 419–433, https://doi.org/10.1016/S0079-6611(03)00033-8.

Shchepetkin, A. F., and J. C. McWilliams, 2005: The Regional Oceanic Modeling System (ROMS): A split-explicit, free-surface, topography-following-coordinate oceanic model. *Ocean Modell.*, **9**, 347–404, https://doi.org/10.1016/j.ocemod.2004.08.002.

——, and ——, 2009: Computational kernel algorithms for fine-scale, multiprocess, longtime oceanic simulations. *Computational Methods for the Atmosphere and the Oceans*, R. M. Temam and J. J. Tribbia, Eds., Vol. 14, *Handbook of Numerical Analysis*, Elsevier, 121–183, https://doi.org/10.1016/S1570-8659(08)01202-0.

Shi, J., and H. Wei, 2007: Evidence of double diffusion in the East China Sea. *J. Mar. Syst.*, **67**, 272–281, https://doi.org/10.1016/j.jmarsys.2006.04.017.

Skamarock, W. C., and Coauthors, 2008: A description of the Advanced Research WRF version 3. NCAR Tech. Note NCAR/TN-475+STR, 113 pp., https://doi.org/10.5065/D68S4MVH.

Stern, M. E., 1960: The "salt-fountain" and thermohaline convection. *Tellus*, **12**, 172–175, https://doi.org/10.3402/tellusa.v12i2.9378.

St. Laurent, L., A. C. Naveira Garabato, J. R. Ledwell, A. M. Thurnherr, J. M. Toole, and A. J. Watson, 2012: Turbulence and diapycnal mixing in Drake Passage. *J. Phys. Oceanogr.*, **42**, 2143–2152, https://doi.org/10.1175/JPO-D-12-027.1.

Talley, L., G. Pickard, W. Emery, and J. Swift, 2011: *Descriptive Physical Oceanography: An Introduction*. Academic Press, 560 pp.

Tanaka, T., I. Yasuda, H. Onishi, H. Ueno, and M. Masujima, 2015: Observations of current and mixing around the shelf break in Pribilof Canyon in the Bering Sea. *J. Oceanogr.*, **71**, 1–17, https://doi.org/10.1007/s10872-014-0256-2.

Tippins, D., and M. Tomczak, 2003: Meridional Turner angles and density compensation in the upper ocean. *Ocean Dyn.*, **53**, 332–342, https://doi.org/10.1007/s10236-003-0056-5.

Turner, J. S., 1973: *Buoyancy Effects in Fluids*. Cambridge Monographs on Mechanics, Vol. 60, Cambridge University Press, 367 pp.

Ullman, D. S., and D. Hebert, 2014: Processing of underway CTD data. *J. Atmos. Oceanic Technol.*, **31**, 984–998, https://doi.org/10.1175/JTECH-D-13-00200.1.

Umlauf, L., and H. Burchard, 2003: A generic length-scale equation for geophysical turbulence models. *J. Mar. Res.*, **61**, 235–265, https://doi.org/10.1357/002224003322005087.

Van Camp, L., L. Nykajer, E. Mittelsaedt, and P. Schlittenhardt, 1991: Upwelling and boundary circulation off northwest Africa as depicted by infrared and visible satellite observations. *Prog. Oceanogr.*, **26**, 357–402, https://doi.org/10.1016/0079-6611(91)90012-B.

Verhoef, A., M. Portabella, and A. Stoffelen, 2012: High-resolution ASCAT scatterometer winds near the coast. *IEEE Trans. Geosci. Remote Sens.*, **50**, 2481–2487, https://doi.org/10.1109/TGRS.2011.2175001.

Warner, J. C., C. R. Sherwood, H. G. Arango, and R. P. Signell, 2005: Performance of four turbulence closure models implemented using a generic length scale method. *Ocean Modell.*, **8**, 81–113, https://doi.org/10.1016/j.ocemod.2003.12.003.

——, B. Butman, and P. S. Dalyander, 2008a: Storm-driven sediment transport in Massachusetts Bay. *Cont. Shelf Res.*, **28**, 257–282, https://doi.org/10.1016/j.csr.2007.08.008.

——, C. R. Sherwood, R. P. Signell, C. K. Harris, and H. G. Arango, 2008b: Development of a three-dimensional, regional, coupled wave, current, and sediment-transport model. *Comput. Geosci.*, **34**, 1284–1306, https://doi.org/10.1016/j.cageo.2008.02.012.

——, B. Armstrong, R. He, and J. B. Zambon, 2010: Development of a Coupled Ocean–Atmosphere–Wave–Sediment Transport (COAWST) modeling system. *Ocean Modell.*, **35**, 230–244, https://doi.org/10.1016/j.ocemod.2010.07.010.

Xie, S.-P., W. T. Liu, Q. Liu, and M. Nonaka 2001: Far-reaching effects of the Hawaiian Islands on the Pacific Ocean-atmosphere system. *Science*, **292**, 2057–2060, https://doi.org/10.1126/science.1059781.

Yang, Y., S. P. Xie, and J. Hafner, 2008: The thermal wake of Kauai Island: Satellite observations and numerical simulations. *J. Climate*, **21**, 4568–4586, https://doi.org/10.1175/2008JCLI1895.1.

——, R. Verzicco, and D. Lohse, 2016: From convection rolls to finger convection in double-diffusive turbulence. *Proc. Natl. Acad. Sci. USA*, **113**, 69–73, https://doi.org/10.1073/pnas.1518040113.

You, Y., 2002: A global ocean climatological atlas of the Turner angle: Implications for double-diffusion and water-mass structure. *Deep-Sea Res. I*, **49**, 2075–2093, https://doi.org/10.1016/S0967-0637(02)00099-7.

Zodiatis, G., and G. P. Gasparini, 1996: Thermohaline staircase formations in the Tyrrhenian Sea. *Deep-Sea Res. I*, **43**, 655–678, https://doi.org/10.1016/0967-0637(96)00032-5.